Laser-induced ultrafast spin injection in all-semiconductor magnetic CrI$_3$/WSe$_2$ heterobilayer

Yilv Guo,[1,2] Yehui Zhang,[1] Qinglong Liu,[2] Zhaobo Zhou,[3] Junjie He,[3] Shijun Yuan,[1] Thomas Heine[2*] and Jinlan Wang[1,4*]*

[1] Key Laboratory of Quantum Materials and Devices of Ministry of Education, School of Physics, Southeast University, Nanjing 211189, China

[2] Faculty of Chemistry and Food Chemistry, TU Dresden, Dresden 01069, Germany

[3] Department of Physical and Macromolecular Chemistry, Faculty of Science, Charles University in Prague, Prague 12843, Czech Republic

[4] Suzhou Laboratory, Suzhou 215004, People's Republic of China

TOC
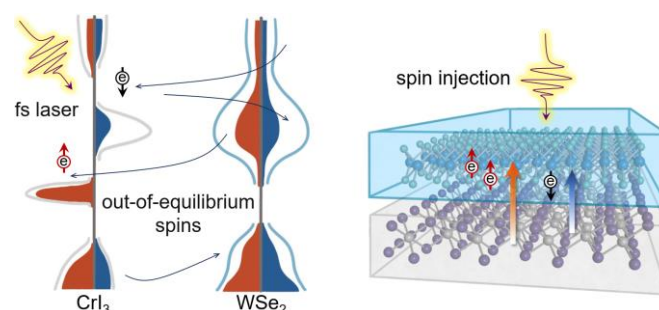
ABSTRACT

Spin injection stands out as a crucial method employed for initializing, manipulating, and measuring the spin state of electrons, which are fundamental to the creation of qubits in quantum computing. However, ensuring efficient spin injection while maintaining compatibility with standard semiconductor processing techniques is a significant challenge. Herein, we demonstrate the capability of inducing an ultrafast spin injection into a WSe_2 layer from a magnetic CrI_3 layer on a femtosecond time scale, achieved through real-time time-dependent density functional theory calculations upon a laser pulse. Following the peak of the magnetic moment in the CrI_3 sublayer, the magnetic moment of the WSe_2 layer reaches a maximum of 0.89 μ_B (per unit cell containing 4 WSe_2 and 1 CrI_3 units). During the spin dynamic, spin-polarized excited electrons transfer from the WSe_2 layer to the CrI_3 layer via a type-II band alignment. The large spin splitting in conduction bands and the difference in the number of spin-polarized local unoccupied states available in the CrI_3 layer lead to a net spin in the WSe_2 layer. Furthermore, we confirmed that the number of empty states, the spin-flip process, and the laser pulse parameters play important roles during the spin injection process. This work highlights the dynamic and rapid nature of spin manipulation in layered all-semiconductor systems, offering significant implications for the development and enhancement of quantum information processing technologies.

KEYWORDS

Introduction

Quantum technology has the potential to revolutionize modern industry by enabling more efficient computers, communication, and sensing devices.[1-3] Manipulating information precisely in quantum systems remains a challenge, crucial for achieving reliable and scalable quantum computing performance.[4] Spin injection is one of the methods used to initialize, manipulate, and measure the spin states of electrons, which are fundamental to the creation of qubits in quantum computing.[5,6] Generally, spin currents are injected into ferromagnetic or diamagnetic materials to manipulate the spins of electrons and control the flow of information via the spin transfer torque effect,[7,8] spin waves,[9,10] spin Hall effect and other spin-orbit coupling mechanisms.[11-13] Since the laser-induced ultrafast demagnetization of Ni film has been observed on the time scale of 1 picosecond (ps), spin manipulation via laser pulse has gained significant attention due to its ability to speed up quantum computations and improve the efficiency of complex calculations.[14-18] One successful case is that, by utilizing a femtosecond (fs) laser excitation, a massive spin transfer can be obtained across a ferromagnet/semiconductor interface, i.e., spin injection into diamagnetic MoS_2 monolayer from the Cobalt layer.[16] This ultrafast manipulation, on the time scale of fs to ps, is significantly faster than many other methods, making it invaluable for studying and exploiting rapid spin dynamics in quantum information processing and high-speed data processing.

So far, most optical spin injection and detection experiments use ferromagnetic metals.[19-21] Optically induced spin transfer,[22] spin-orbit coupling,[23] and spin-flip scattering[24,25] are discovered for the mechanism of ultrafast spin manipulation. The ability to work with all-semiconductor materials provides tunable properties, makes the devices more compatible with existing semiconductor-based

electronics, and leads to more rapid scalability for quantum information processing.[26] The discovered two-dimensional (2D) magnetic semiconductors, such as CrI_3,[27] $CrGeTe_3$,[28] and $CrSBr$,[29, 30] provide a platform for quantum technologies due to their ability to transport both charge and spin efficiently.[31-33] It is a fact that the spin dynamic processes indirectly couple light to spins,[34] the mechanics of light-matter interactions, including effects such as interlayer spin transfer, spin dynamics, and optical spin manipulation, are eager to be explored and exploited to unlock the full potential of 2D all-semiconductor magnetic systems.

In this work, an all-semiconductor CrI_3/WSe_2 heterobilayer, in which the two constituting layers have been widely studied individually, both theoretically and experimentally, is proposed to show great promise for laser-induced spin injection. Although a negligible magnetic proximity effect is revealed on the WSe_2 layer in the ground state via density functional theory (DFT) simulations, an ultrafast enhanced spin polarization can be induced in the WSe_2 sublayer upon a laser pulse by real-time time-dependent density functional theory (rt-TDDFT) calculations. To distinguish the roles of optical excitations and relaxations, we performed rt-TDDFT calculations without spin-orbit coupling (SOC) first. The out-of-equilibrium excited electrons transfer from the WSe_2 to the CrI_3 layer by a type-II band alignment. The spin injection originates from a spin-polarized population of electrons in the WSe_2 sublayer, induced by different numbers of available local unoccupied states in spin-up and spin-down channels of the CrI_3 sublayer. Furthermore, we found that SOC fosters the speed the process. Also the number of empty states, the spin flip and the parameters of the laser pulse are crucial factors that can be used to adjust the spin injection process. This work highlights an exciting prospect of high-speed and ultra-compact architectures for the field of quantum computing.

Results and discussions

A 2 × 2 cell of WSe_2 is matched at the interface with a 1 × 1 cell of CrI_3 (Figure 1a), with a lattice mismatch of 5%. Full geometry optimization resulted in a lattice parameter of 6.81 Å for the CrI_3/WSe_2 heterobilayer. Three different stacking configurations of WSe_2 and CrI_3 heterobilayers have been considered (Figure S1). The relative total energies of the heterostructures demonstrate that type A is the most favorable stacking configuration (Table S1), shown in Figure 1a. The equilibrium distance between the Se and I planes is 3.44 Å and the ground state of the WSe_2 sublayer possesses a small proximity magnetic moment of -0.02 μ_B, which increases to -0.12 μ_B when considering the SOC. The magnetic moment is calculated in per unit cell, which consists of 4 WSe_2 units and 1 CrI_3 unit, except for specific indications.

In the WSe_2/CrI_3 heterostructure, the global valence band maximum (VBM) and the conduction band minimum (CBM) are mainly contributed by WSe_2 and CrI_3 sublayers, respectively, indicating a type II band alignment (Figure 1b). A type-I band alignment is observed in the spin-down channel since both the VBM and CBM are located in the WSe_2 sublayer. The calculated band gap of the WSe_2 layer is 1.11 eV, while the spin-up and spin-down band gaps of the CrI_3 are 1.17 eV and 2.78 eV, respectively. When SOC is taken into account (Figure 1d and 1e), the WSe_2 sublayer of the heterostructure has a direct gap with a giant spin splitting of at the valence band maximum (~0.5 eV) at the K (K′) point. This is in general agreement with previous experimental and theoretical predictions.[35, 36] Moreover, the stacking configurations have negligible effects on electronic band structures (Figure S2 and S3) and magnetic properties (Table S1 and S2) of WSe_2/CrI_3 heterostructures both without and with taking SOC into account.

The global type-II band alignment of WSe_2/CrI_3 heterostructure contribute to efficient spin injection. Additionally, a significant spin-flip gap of approximately 1.5 eV exists in the conduction band of the CrI_3 layer, indicating a large difference in energy between spin-up and spin-down CBM. Upon excitation by a fs laser, the ferromagnetic layer is expected to have a strongly out-of-equilibrium, spin-polarized carrier distribution. When the excited carriers diffuse and relax, the separation and transfer of the electron and hole carriers can be facilitated due to the global type-II band alignment at the interface (Figure 1c). The WSe_2 layer acts as the receiver of the spin-polarized high-energy carriers, which is expected to lead to efficient spin current injection in WSe_2/CrI_3 heterostructures.
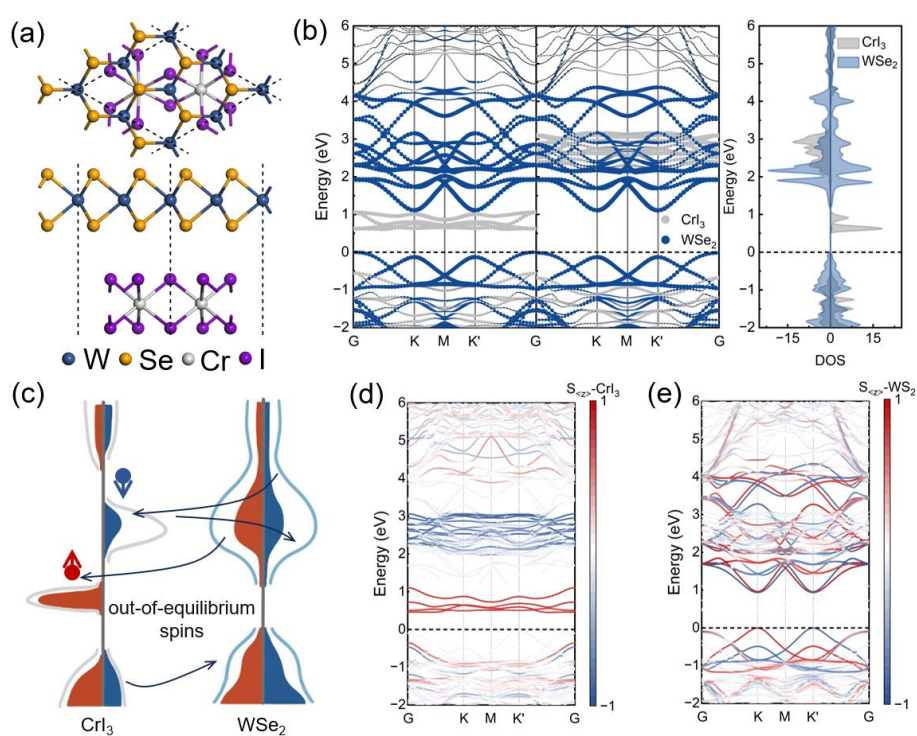

Figure1. (a) Top view and side view of the atomic structure for the CrI_3/WSe_2 heterobilayer. (b) Layer-projected band structures and density of states for CrI_3/WSe_2 heterobilayer without SOC effect. (c) Schematic of spin injection in CrI_3/WSe_2 heterobilayer. Band structures for (d) CrI_3 and (e) WSe_2 sublayers with SOC. The color bar represents projected expectation value of the spin operator S_z on

the spinor wave functions.

Then rt-TDDFT calculations are performed to explore spin injection into the all-semiconductor CrI_3/WSe_2 heterobilayer with an ultra-short laser pulse. A linearly polarized (in-plane polarization) pulse with a photon energy of 1.40 eV, full width at half maximum of 6.04 fs, and a fluence rate of 10.30 mJ/cm^2 is applied as a driven laser field. The spin dynamics are first calculated without SOC to identify the roles of optical excitations and relaxations, as shown in Figure 2. The relative layer-projected magnetic moments presented in Figure 2a reveal that (i) the sublayer of WSe_2 exhibits an obvious increase in magnetic moment, reaching 1.14 μ_B at 52.4 fs; (ii) It happens after the magnetic moment of the CrI_3 sublayer reduced from 5.71 μ_B to 4.58 μ_B at 51.4 fs; (iii) The change of delocalized moment is negligible. According to the element-projected magnetic moments as a function of time (Figure 2b), the enhanced magnetic moment in the WSe_2 layer can be attributed to both W and Se elements. As the global moment remains constant, the laser pulse induces spin injection from CrI_3 to the WSe_2 sublayer.

To verify the spin dynamics, the change of spin-polarized occupation of charge, excited charge in conduction bands (CBs) and valance bands (VBs) are investigated (Figure 2d-2i). Dynamics of occupations for spin-up (Figure 2d) and spin-down (Figure 2g) charges are defined as:

$$\Delta n_{up}(t) = \frac{\Delta n(t) + \Delta M(t)}{2} \quad (1)$$

$$\Delta n_{dn}(t) = \frac{\Delta n(t) - \Delta M(t)}{2} \quad (2)$$

where $\Delta n(t) = n(t) - n(t=0)$ is the time-dependent change of the local charge as compared to the initial charge. The change of the local spin moment is defined as $\Delta M(t) = M(t) - M(t = 0)$. During the spin

dynamic process, three distinct periods can be determined. In the first period (labeled as I), which lasts from 7.6 to 26.9 fs, the laser pulse causes an increase in the spin-up electron of W, the spin-down electron of Cr, and the delocalized states, while a decrease in spin electron for the others. During 26.9 to 51.2 fs period (labeled as II), there is a reversable increase of spin-down electrons of W atoms. After 51.2 fs (labeled as III), there is an oscillation of Cr_up and I_up electrons, along with a reduction of I_down and an increase in Cr_down electron spins.

The spin-maintained optical excitations (labeled as ① in Figure 2c) and relaxations (pathways are labeled as ② and ③ for spin-up channel, ④ and ⑤ for spin-down channel) are responsible for the spin injection. The recombination and lattice heating can be neglected because the characteristic times of these processes (> 100 fs) are much higher than the pulse duration.[37] When exposed to a laser pulse of 1.4 eV, both the WSe_2 and CrI_3 sublayers experience an excitation of electrons from VBs to CBs. This can be confirmed by observing an increase in the number of excited charges in CBs, a decrease in the number of charges in VBs (as shown in Figures 2e-2h), and even the appearance of high-energy delocalized states up to 6 eV (as seen in Figures S4 and S5). Notably, there are very few spin-down electrons that are reduced in CBs of the CrI_3 layer. Therefore, the intralayer excitation thus plays a dominant role (Figure 2j) during the (I) time period.

During the (II) time period, both intralayer excitation and interlayer transfer dominate as high-energy electrons relax from 6.0 eV to 0.5-4.0 eV (Figure 2k). Generally, electrons and holes are separated into CrI_3 and WSe_2 sublayers (Figure 2c) during the relaxation process, respectively, owing to the intrinsic type-II band alignment of the spin-up channel. Thus, excited electrons quickly fill local spin-up CBs (~ 0.4-1.1 eV as shown in Figure S4) of the CrI_3 sublayer, leading to a flat plateau ((II)

time period in Figure 2e). The electrons and holes relax to the WSe$_2$ sublayer due to type-I band alignment in the spin-down channel. Enhanced spin-down excited charges are observed in the CBs of the CrI$_3$ layer (Figure 2h), owing to the available empty states available for excited electrons to relax into the unoccupied bands.

In the (III) period, the spin-up electrons in CrI$_3$ occupy high-energy bands around 4.0 to 6.0 eV (Figure S4). This leads to the accumulation of excited states in CBs, giving rise to the formation of a new plateau ((III) time period in Figure 2e). The oscillation of Cr_up and I_up charges mainly originate from their competition for available unoccupied states. The spin-down local unoccupied states of CrI$_3$ (~ 1.6-3.1 eV) are mainly dominated by Cr atoms (Figure S2c). These states continue to gain electrons and reach a plateau at t $\approx$ 51.24 fs (Figure 2h). This results in the greatly enhanced Cr_down spin electrons, which in turn reduces the magnetic moment of Cr atoms. the available local unoccupied states (0.5 to 4.0 eV) in the CrI$_3$ sublayer play an important role in the dominant accumulation of spin-polarized electrons in the WSe$_2$ layer according to the entire process. The out-of-equilibrium excited electrons induce a spin population difference between spin-up and spin-down electrons in the WSe$_2$ sublayer (Figure 2l).
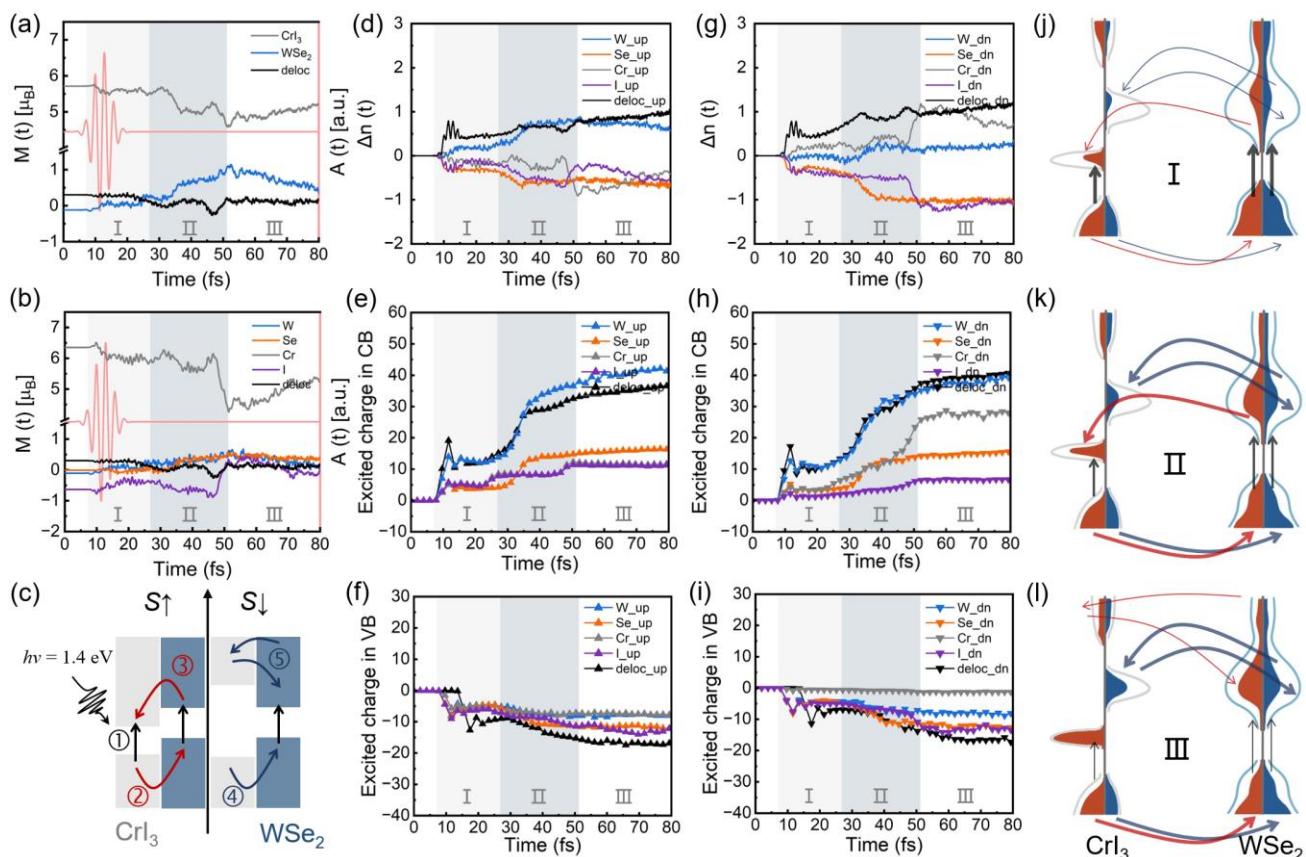
Figure 2. (a) The dynamics of the local moment on CrI₃ layer and Wse₂ layer (per unit cell containing 4 WSe₂ and 1 CrI₃ units), and of the delocalized moment at various fluence rates for the CrI₃/WSe₂ heterobilayer, calculated without SOC by using a linearly polarized (in-plane polarization) pulse. (b) Time evolution of the absolute total local moment of W, Se, Cr, and I atoms, respectively. (c) Schematics of optical excitations and relaxations in the CrI₃/WSe₂ heterobilayer. ① denotes the optical excitation process. Relaxation pathways are labeled as ② and ③ for spin-up channel, ④ and ⑤ for spin-down channel. The time-dependent change in the (d) spin-up and (g) spin-down electrons on each element (and of the delocalized electrons) relative to the ground-state for the CrI₃/WSe₂ heterobilayer. Excited charge in the (e,f) spin-up and (h,i) spin-down channels projected on each element, below and above the ground state (E = 0 eV) compared with that at the initial time (t = 0) respectively. (j-l) Schematic diagram of electron population during spin-injection process without SOC. The black and

blue arrows represent the processes of transition and relaxation, and the thickness denotes the strength.

Considering the crucial role of SOC in spin dynamics reported in previous studies of magnetic metals/nonmagnetic materials,[38, 39] the time-dependent magnetic moments with SOC were calculated, as shown in Figure 3. A spin-flip process is observed as the total magnetic moment increases and then decreases after 40.0 fs (Figure 3a). The magnetic moment of the CrI_3 layer increases up to a peak of 7.29 μ_B at 33.6 fs from the initial 5.75 μ_B. The magnetic moment of the WSe_2 layer reaches its maximum of 0.89 μ_B at 40.4 fs. After 30 fs, the magnetic moment of delocalized states decays rapidly. To investigate the effect of SOC on spin dynamics, the layer and orientational projected magnetic moments as a function of time are displayed in Figure 4a and 4b. The in-plane magnetic moment is averaged over all different species of atoms, i.e.,

$$\overline{m_{xy}} = \frac{1}{N_i} \sum_j^{N_i} \sqrt{m_{j,x}^2 + m_{j,y}^2} \quad (3)$$

where N_i is the number of different kinds of atoms, $m_{j,x}$ and $m_{j,y}$ are the x and y components of the jth atoms. Before 55 fs, significant magnetic orientations are mainly along the z direction, as shown in Figure 4a and 4b. Based on the element projected spin dynamics (Figure S6), the magnetic moment change in the CrI_3 layer mainly originates from the Cr atoms, and the enhanced magnetic moment in the WSe_2 layer is primarily due to the contribution of W. After 55 fs, the orientation of spin in the WSe_2 layer is inclined (Figure S7), and a considerable component of the in-plane magnetic moment is shown in Figure 4b. This might be attributed to the competition between electron spin orientations, which are dependent on optical selection rules for interband transitions.[40] Further investigations are required to confirm this finding.
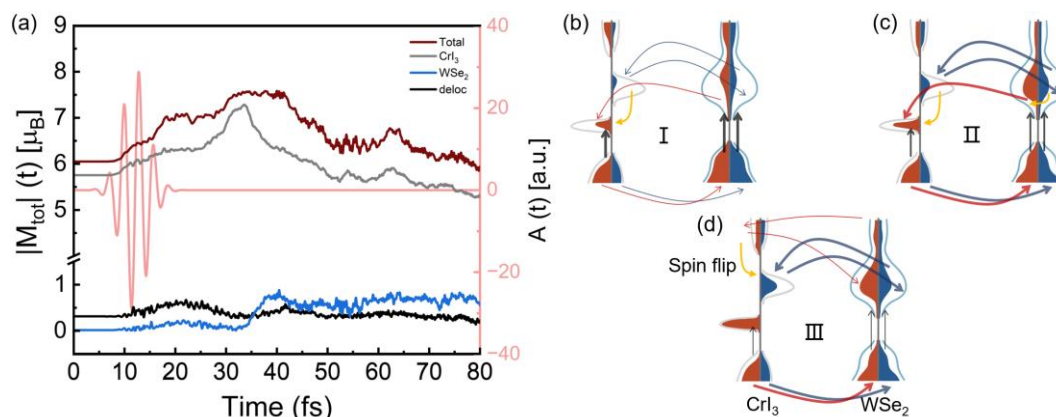
Figure 3. (a) The dynamics of the absolute local moment on CrI_3 layer and WSe_2 layer (per unit cell containing 4 WSe_2 and 1 CrI_3 units), and of the delocalized moment for the CrI_3/WSe_2 heterobilayer, calculated with SOC. (b-d) Schematic diagram of electron population during spin-injection process. (b) Initial out-of-equilibrium electronic distribution generated by the laser absorption. (c) Due to a type-II band alignment, the local spin-up conduction bands of CrI_3 layer are filling up. (d) The full-filled local spin-up d-band of CrI_3 layer blocks electron transfer, leading to spin polarization of the injection in WSe_2 layer.

To provide insight into the mechanism of the magnetic moment change, the time-dependent spin-polarized charge occupation along the z direction, and the change of excited charge in CBs and VBs are illustrated in Figure 4. The definitions of spin up and spin down are not valid for noncollinear magnetic systems, where the spin moment is no longer a good quantum number. However, the magnetization density can be treated as a vector field, and the eigenspinors in this representation are of pure spin-up or spin-down character.[41] As the magnetic orientation remains almost collinear behavior before 55 fs, the definitions of Δn_{up} and Δn_{dn} are still used to understand the mechanisms. The main process can still be divided into three time periods. As shown in Figure 4e-4h, Figure S8 and S9: (i) The (I) time period is dominated by intralayer excitation, where electrons are excited from VBs

to CBs and high-energy delocalized states in separate layers; (ii) In the (II) period, intralayer excitation and interlayer transfer enable election occupations in local spin-up bands of the CrI_3 layer around 0.5-1.4 eV. In contrast to the results without SOC (Figure 2g), there is a reduced population of spin-down charges of CrI_3 and WSe_2 layers (Figure 4d), which indicates a spin-flip process; (iii) During the (III) period, the unoccupied spin-down states of CrI_3 are gradually filled up between 1.8-3.2 eV (Figure S9). The magnetic moment of the CrI_3 layer decreases due to the increased spin-down electron spins while reduced spin-up electrons (Figure 4c and 4d).

To reveal the spin-flip process, the changes of the spin-polarized electrons at 7.7, 13.5, 27.0, 33.5, and 40.6 fs are selected from (I), (II) and (III) time scales, as summarized in Tables S3-S5. It can be observed that the spin-flip process at the I time scale is mainly caused by the intralayer spin-flip process (Figure 3b), which involves the transfer of electrons from I_down to I_up. In the II timescale, the spin-flip process occurs through both intralayer and interlayer ways, specifically from Cr_down to Cr_up electrons via direct and WSe_2-layer mediated relaxation process (Figure 3c). As shown in Figure 3d, the loss of spin-up electrons in the CrI_3 layer can be excited to high-energy delocalized states, and partly flip into spin-down states through high-energy states ranging from 4 eV to 6 eV. Compared to the evolution of electronic occupied states, the net spin injection of WSe_2 results mostly from the transfer of spin-down electrons (0.76 e/atom) and the negligible transfer of spin-up electrons (0.01 e/atom).
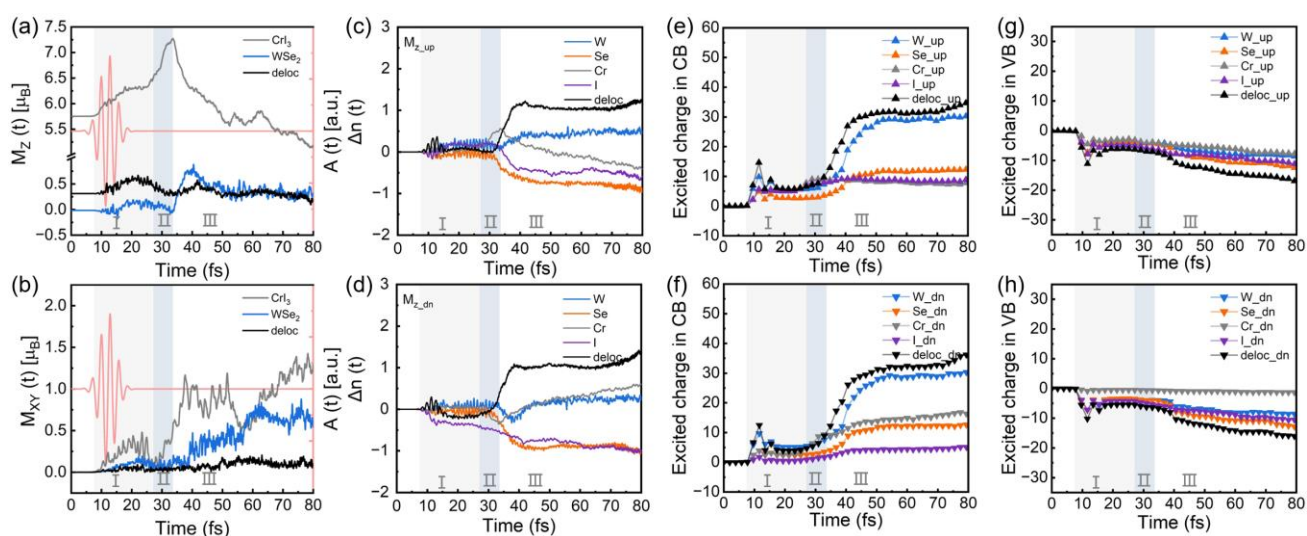
Figure 4. Time evolution of the (a) out-of-plane and (b) in-plane local moment of CrI$_3$ layer, WSe$_2$ layer, and of the delocalized state for the CrI$_3$/WSe$_2$ heterobilayer (per unit cell containing 4 WSe$_2$ and 1 CrI$_3$ units). The time-dependent change along z direction in the (c) spin-up and (d) spin-down electrons on each element (and of the delocalized electrons) relative to the ground state for the CrI$_3$/WSe$_2$ heterobilayer. Excited charge in the (e,g) spin-up and (f,h) spin-down channels projected on each element, below and above the ground state (E = 0 eV) compared with that at the initial time (t = 0) respectively.

To assess the impact of laser pulse parameters on the efficiency of spin excitation in CrI$_3$/WSe$_2$ heterojunction, the spin dynamics under various laser pulses are studied. 1.40 eV laser pulses, full width at half maximum of 6.04 fs, and fluence rates of 10.3/16.1 mJ/cm^2, are analyzed as shown in Figure S10. The magnetic moment and spin injection are influenced by laser parameters, indicating the rates of unoccupied states available to excited electrons and the strength of SOC-induced spin flip can be tuned by laser parameters. Significantly, spin dynamics exhibit a remarkable uniformity, indicating a consistent underlying mechanism. Consequently, the utilization of diverse laser pulses emerges as a promising avenue for tuning and optimizing the intricate process of spin injection.

Moreover, stable spin injection is exclusively induced in the CrI_3/WSe_2 heterobilayer (Figure S11), as the spin moment undergoes pronounced oscillations within the monolayer of WSe_2.

Conclusion

In summary, DFT and rt-TDDFT simulations were performed for the ground-state magnetic properties and the spin injection process, respectively, in the all-semiconductor CrI_3/WSe_2 heterobilayer. The DFT calculations indicate that the magnetic proximity effects are weak in the ground state. Interestingly, an effective spin injection can be induced from the magnetic CrI_3 sublayer into the WSe_2 sublayer, triggered by a laser pulse within a few femtoseconds. The spin-polarized out-of-equilibrium excited electrons transfer from the WSe_2 layer to the CrI_3 layer, facilitated by a type-II band alignment. The generation of a spin-polarized population of electrons in the WSe_2 sublayer is driven by a large spin splitting in CBs and the presence of available local unoccupied states in two spin channels of the CrI_3 sublayer. In addition, the efficiency of the spin injection process is highly relevant to the availability of unoccupied states and the spin flip induced by SOC, which can be manipulated and controlled by various laser pulses. The all-semiconductor structure allows for ultrafast spin injection into the diamagnetic sublayer, with a high likelihood of seamless integration into modern electronics. This creates a versatile platform for optical control of spin transport and manipulation, particularly relevant for the advancement of quantum computing technologies.

Methods

All the density functional theory (DFT) computations were implemented with the Vienna ab initio simulation package (VASP),[42] employing the projector augmented wave method.[43] The generalized gradient approximation exchange and correlation functional, developed by Perdew, Burke, and

Ernzerhof (PBE) was used.[44] An energy cutoff of 400 eV was set, and all the structures were fully optimized until satisfying a force criterion of 0.01 eV/Å. A k-mesh of $7 \times 7 \times 1$ was used for WSe_2/CrI_3 heterostructures. The structure was inserted a large distance of vacuum space greater than 15 Å to eliminate the interaction between two periodic units. The semiempirical correction scheme of Grimme, DFT-D3,[45] was applied to treat the vdW weak interaction. In order to better describe the correlation effects for Cr-d orbitals, an effective Hubbard U of 3 eV was considered.[46]

To investigate the behavior of spin and charge in materials when exposed to ultrafast laser pulses, , the non-collinear spin-dependent version of real-time time-dependent density functional theory (rt-TDDFT) was used. In this approach, the Kohn-Sham (KS) orbitals are treated as Pauli spinors that are determined by the equations:

$$i \frac{\partial \Psi_j(r,t)}{\partial t} = \left[\frac{1}{2}\left(-i\nabla + \frac{1}{c}\boldsymbol{A}_{ext}(t)\right)^2 + v_s(\boldsymbol{r},t) + \frac{1}{2c}\sigma \cdot \boldsymbol{B}_s(\boldsymbol{r},t) + \frac{1}{4c^2}\sigma \cdot (\nabla v_s(\boldsymbol{r},t) \times -i\nabla) \right] \Psi_j(\boldsymbol{r},t) \quad (4)$$

where $\mathbf{A}_{ext}(t)$ represents the vector potential of the applied laser field, and σ are the Pauli matrices. The KS effective potential $v_s(\mathbf{r}, t) = v_{ext}(\mathbf{r}, t) + v_H(\mathbf{r}, t) + v_{xc}(\mathbf{r}, t)$ is the sum of the external potential v_{ext}, the classical electrostatic Hartree potential v_H and the exchange-correlation (XC) potential v_{xc}. The KS magnetic field can be expressed as $\mathbf{B}_s(\mathbf{r}, t) = \mathbf{B}_{ext}(t) + \mathbf{B}_{xc}(\mathbf{r}, t)$, where $\mathbf{B}_{ext}(t)$ refers to the magnetic field of the applied laser pulse plus possibly an additional magnetic field, and $\mathbf{B}_{xc}(\mathbf{r}, t)$ is the XC magnetic field. The final term is the spin-orbit coupling term. The nuclei of the system is fixed during the calculations.

The spin current density tensor, $\overleftrightarrow{\boldsymbol{J}}(\mathbf{r})$, is defined as the expectation value of the operator $\hat{\sigma}\hat{j}$ where the Pauli spin matrices are denoted by σ are and $\hat{j}$ represents the usual electronic current density operator that covers both paramagnetic and diamagnetic contributions. In order to understand

the nature of this tensor, the equation of motion of the magnetization density is:

$$\frac{\partial m(t)}{\partial t} = -\nabla \cdot \overleftrightarrow{J}(\mathbf{r}) - \frac{1}{c}\boldsymbol{m}(\boldsymbol{r}) \times \boldsymbol{B}_s(\boldsymbol{r}) \qquad (5)$$

In the absence of an external magnetic field, and a locally collinear XC functional, adiabatic local spin density approximation (ALSDA), is used, the second term on the right becomes zero. As a result, this equation simplifies into a continuity equation for the magnetization density.

To perform the laser-induced dynamic calculations, the full potential linearized augmented-plane-wave method was used, as implemented in the ELK code.[47] In all calculations, a regular mesh in **k**-space of 4 × 4 × 1 grid points, a smearing width of 0.136 eV, and a time step of Δt = 0.2 au were employed for the time-propagation algorithm. A linearly polarized (in-plane polarization) pulse is applied as a driven laser field. A benchmark of band structures calculated by VASP and ELK is given in Figure S12, which shows similar results.

ASSOCIATED CONTENT

Supporting Information

Different stacking configurations for WSe_2/CrI_3 heterostructures; Element-resolved band structures and density of states without and with SOC; Element-projected transition states as a function of time without and with SOC; Selected snapshot of spin orientations; Spin dynamics at various fluence rates; Spin dynamics for CrI_3 and WSe_2 monolayers with SOC; Benchmark of band structures between VASP and ELK codes; Relative energies and local magnetic moments for different stacking constructions without and with SOC; Magnetic anisotropy energies; Selected time-dependent change along the z direction of the spin-up and spin-down electrons.

AUTHOR INFORMATION

Corresponding Author

Jinlan Wang - Key Laboratory of Quantum Materials and Devices of Ministry of Education, School of Physics, Southeast University, Nanjing 211189, China; Suzhou Laboratory, Suzhou 215004, People's Republic of China; E-mail: jlwang@seu.edu.cn

Thomas Heine - Faculty of Chemistry and Food Chemistry, TU Dresden, Dresden 01069, Germany; E-mail: Thomas.Heine@tu-dresden.de

Shijun Yuan - Key Laboratory of Quantum Materials and Devices of Ministry of Education, School of Physics, Southeast University, Nanjing 211189, China; E-mail: siesta@seu.edu.cn

Authors

Yilv Guo - Key Laboratory of Quantum Materials and Devices of Ministry of Education, School of Physics, Southeast University, Nanjing 211189, China; Faculty of Chemistry and Food Chemistry, TU Dresden, Dresden 01069, Germany

Yehui Zhang - Key Laboratory of Quantum Materials and Devices of Ministry of Education, School of Physics, Southeast University, Nanjing 211189, China

Qinglong Liu - Faculty of Chemistry and Food Chemistry, TU Dresden, Dresden 01069, Germany

Zhaobo Zhou - Department of Physical and Macromolecular Chemistry, Faculty of Science, Charles University in Prague, Prague 12843, Czech Republic

Junjie He - Department of Physical and Macromolecular Chemistry, Faculty of Science, Charles University in Prague, Prague 12843, Czech Republic

Notes

The authors declare that they have no competing interests.

REFERENCES

1. Cai, X. X., Connors, E. J., Edge, L. F., Nichol, J. M., Coherent spin-valley oscillations in silicon. *Nat. Phys.* **2023,** *19*, 386–393.
2. Wang, J. W., Sciarrino, F., Laing, A., Thompson, M. G., Integrated photonic quantum technologies. *Nat. Photonics* **2020,** *14*, 273-284.
3. Montblanch, A. R. P., Barbone, M., Aharonovich, I., Atatüre, M., Ferrari, A. C., Layered materials as a platform for quantum technologies. *Nat. Nanotechnol.* **2023,** *18*, 555-571.
4. Acín, A., Bloch, I., Buhrman, H., Calarco, T., Eichler, C., Eisert, J., Esteve, D., Gisin, N., Glaser, S. J., Jelezko, F., Kuhr, S., Lewenstein, M., Riedel, M. F., Schmidt, P. O., Thew, R., Wallraff, A., Walmsley, I., Wilhelm, F. K., The quantum technologies roadmap: a European community view. *New J. Phys.* **2018,** *20*, 080201.
5. Dusanowski, L., Nawrath, C., Portalupi, S. L., Jetter, M., Huber, T., Klembt, S., Michler, P., Höfling, S., Optical charge injection and coherent control of a quantum-dot spin-qubit emitting at telecom wavelengths. *Nat. Commun.* **2022,** *13*, 748.
6. Kulkarni, A., Prajapati, S., Kaushik, B. K., Transmission Coefficient Matrix Modeling of Spin-Torque-Based
-Qubit Architecture. *IEEE Trans. Very Large Scale Integr. VLSI Syst.* **2018,** *26*, 1461-1470.
7. Davidson, A., Amin, V. P., Aljuaid, W. S., Haney, P. M., Fan, X., Perspectives of electrically generated spin currents in ferromagnetic materials. *Phys. Lett. A* **2020,** *384*, 126228.
8. Choi, G. M., Oh, J. H., Lee, D. K., Lee, S. W., Kim, K. W., Lim, M., Min, B. C., Lee, K. J., Lee, H. W., Optical spin-orbit torque in heavy metal-ferromagnet heterostructures. *Nat. Commun.* **2020,** *11*, 1482.
9. Razdolski, I., Alekhin, A., Ilin, N., Meyburg, J. P., Roddatis, V., Diesing, D., Bovensiepen, U., Melnikov, A., Nanoscale interface confinement of ultrafast spin transfer torque driving non-uniform spin dynamics. *Nat. Commun.* **2017,** *8*, 15007.
10. Go, G., Lee, S., Kim, S. K., Generation of nonreciprocity in gapless spin waves by chirality injection. *Phys. Rev. B* **2022,** *105*, 134401.
11. Tschirhart, C. L., Redekop, E., Li, L., Li, T., Jiang, S., Arp, T., Sheekey, O., Taniguchi, T., Watanabe, K., Huber, M. E., Mak, K. F., Shan, J., Young, A. F., Intrinsic spin Hall torque in a moiré Chern magnet.

Nat. Phys. **2023,** *19*, 807-813.

12. Tao, Z., Shen, B. W., Zhao, W. J., Hu, N. C., Li, T. X., Jiang, S. W., Li, L. Z., Watanabe, K., Taniguchi, T., MacDonald, A. H., Shan, J., Mak, K. F., Giant spin Hall effect in AB-stacked MoTe/WSe bilayers. *Nat. Nanotechnol.* **2023**.

13. Maekawa, S., MAGNETISM A flood of spin current. *Nat. Mater.* **2009,** *8*, 777-778.

14. Beaurepaire, E., Merle, J. C., Daunois, A., Bigot, J. Y., Ultrafast spin dynamics in ferromagnetic nickel. *Phys. Rev. Lett.* **1996,** *76*, 4250-4253.

15. Kholid, F. N., Hamara, D., Bin Hamdan, A. F., Antonio, G. N., Bowen, R., Petit, D., Cowburn, R., Pisarev, R. V., Bossini, D., Barker, J., Ciccarelli, C., The importance of the interface for picosecond spin pumping in antiferromagnet-heavy metal heterostructures. *Nat. Commun.* **2023,** *14*, 538.

16. Cheng, L., Wang, X. B., Yang, W. F., Chai, J. W., Yang, M., Chen, M. J., Wu, Y., Chen, X. X., Chi, D. Z., Goh, K. E. J., Zhu, J. X., Sun, H. D., Wang, S. J., Song, J. C. W., Battiato, M., Yang, H., Chia, E. E. M., Far out-of-equilibrium spin populations trigger giant spin injection into atomically thin MoS_2. *Nat. Phys.* **2019,** *15*, 347–351.

17. Battiato, M., Held, K., Ultrafast and Gigantic Spin Injection in Semiconductors. *Phys. Rev. Lett.* **2016,** *116*, 196601.

18. Kimel, A., Zvezdin, A., Sharma, S., Shallcross, S., de Sousa, N., García-Martín, A., Salvan, G., Hamrle, J., Stejskal, O., McCord, J., Tacchi, S., Carlotti, G., Gambardella, P., Salis, G., Münzenberg, M., Schultze, M., Temnov, V., Bychkov, I. V., Kotov, L. N., Maccaferri, N., Ignatyeva, D., Belotelov, V., Donnelly, C., Rodriguez, A. H., Matsuda, I., Ruchon, T., Fanciulli, M., Sacchi, M., Du, C. R., Wang, H. L., Armitage, N. P., Schubert, M., Darakchieva, V., Liu, B. L., Huang, Z. Y., Ding, B. F., Berger, A., Vavassori, P., The 2022 magneto-optics roadmap. *J Phys D Appl Phys* **2022,** *55*, 463003.

19. Min, K. H., Lee, D. H., Choi, S. J., Lee, I. H., Seo, J., Kim, D. W., Ko, K. T., Watanabe, K., Taniguchi, T., Ha, D. H., Kim, C., Shim, J. H., Eom, J., Kim, J. S., Jung, S., Tunable spin injection and detection across a van der Waals interface. *Nat. Mater.* **2022,** *21*, 1144–1149.

20. Elliott, P., Eschenlohr, A., Chen, J. H., Shallcross, S., Bovensiepen, U., Dewhurst, J. K., Sharma, S., Transient Spin Injection Efficiencies at Ferromagnet-Metal Interfaces. *Adv. Mater. Interfaces* **2022,** *9*, 2201233.

21. Laterza, S., Caretta, A., Bhardwaj, R., Lammini, R. F., Moras, P., Jugovac, M., Rajak, P., Islam, M., Ciancio, R., Bonanni, V., Casarin, B., Simoncig, A., Zangrando, M., Ribic, P. R., Penco, G., De Ninno, G., Giannessi, L., Demidovich, A., Danailov, M., Parmigiani, F., Malvestuto, M., All-optical spin injection in silicon investigated by element-specific time-resolved Kerr effect. *Optica* **2022,** *9*, 1333-1338.

22. Dewhurst, J. K., Elliott, P., Shallcross, S., Gross, E. K. U., Sharma, S., Laser-Induced Intersite Spin Transfer. *Nano Lett.* **2018,** *18*, 1842-1848.

23. Krieger, K., Dewhurst, J. K., Elliott, P., Sharma, S., Gross, E. K. U., Laser-Induced Demagnetization at Ultrashort Time Scales: Predictions of TDDFT. *J. Chem. Theory Comput.* **2015,** *11*, 4870-4874.

24. Turgut, E., La-o-Vorakiat, C., Shaw, J. M., Grychtol, P., Nembach, H. T., Rudolf, D., Adam, R., Aeschlimann, M., Schneider, C. M., Silva, T. J., Murnane, M. M., Kapteyn, H. C., Mathias, S., Controlling the Competition between Optically Induced Ultrafast Spin-Flip Scattering and Spin Transport in Magnetic Multilayers. *Phys. Rev. Lett.* **2013,** *110*, 197201.

25. Mann, A., Walowski, J., Münzenberg, M., Maat, S., Carey, M. J., Childress, J. R., Mewes, C., Ebke, D., Drewello, V., Reiss, G., Thomas, A., Insights into Ultrafast Demagnetization in Pseudogap Half-

Metals. *Phys. Rev. X* **2012,** *2*, 041008.

26. Zhang, X., Li, H. O., Cao, G., Xiao, M., Guo, G. C., Guo, G. P., Semiconductor quantum computation. *Natl. Sci. Rev.* **2019,** *6*, 32-54.

27. Huang, B., Clark, G., Navarro-Moratalla, E., Klein, D. R., Cheng, R., Seyler, K. L., Zhong, D., Schmidgall, E., McGuire, M. A., Cobden, D. H., Yao, W., Xiao, D., Jarillo-Herrero, P., Xu, X., Layer-Dependent Ferromagnetism in a Van der Waals Crystal down to the Monolayer Limit. *Nature* **2017,** *546*, 270-273.

28. Gong, C., Li, L., Li, Z., Ji, H., Stern, A., Xia, Y., Cao, T., Bao, W., Wang, C., Wang, Y., Qiu, Z. Q., Cava, R. J., Louie, S. G., Xia, J., Zhang, X., Discovery of Intrinsic Ferromagnetism in Two-Dimensional Van der Waals Crystals. *Nature* **2017,** *546*, 265-269.

29. Lee, K., Dismukes, A. H., Telford, E. J., Wiscons, R. A., Wang, J., Xu, X., Nuckolls, C., Dean, C. R., Roy, X., Zhu, X., Magnetic Order and Symmetry in the 2D Semiconductor CrSBr. *Nano Lett.* **2021,** *21*, 3511-3517.

30. Guo, Y., Zhang, Y., Yuan, S., Wang, B., Wang, J., Chromium Sulfide Halide Monolayers: Intrinsic Ferromagnetic Semiconductors with Large Spin Polarization and High Carrier Mobility. *Nanoscale* **2018,** *10*, 18036-18042.

31. Soriano, D., Katsnelson, M. I., Fernandez-Rossier, J., Magnetic Two-Dimensional Chromium Trihalides: A Theoretical Perspective. *Nano Lett.* **2020,** *20*, 6225-6234.

32. Zhang, X. W., Zhou, Z. B., Yu, X., Guo, Y. L., Chen, Y. F., Wang, J. L., Ferroelectric Control of Polarity of the Spin-polarized Current in Van Der Waals Multiferroic Heterostructures. *Adv. Funct. Mater.* **2023,** *33*, 2301353.

33. Guo, Y., Yu, X., Zhang, Y. H., Zhang, X. W., Yuan, S. J., Li, Y. F., Yang, S. Y. A., Wang, J. L., 2D Multiferroicity with Ferroelectric Switching Induced Spin-Constrained Photoelectricity. *ACS Nano* **2022,** *16*, 11174-11181.

34. Hanson, R., Awschalom, D. D., Coherent manipulation of single spins in semiconductors. *Nature* **2008,** *453*, 1043–1049.

35. Ge, M., Wang, H., Wu, J., Si, C., Zhang, J., Zhang, S., Enhanced valley splitting of WSe2 in twisted van der Waals WSe2/CrI3 heterostructures. *npj Comput. Mater.* **2022,** *8*, 32.

36. Wilson, N. R., Nguyen, P. V., Seyler, K., Rivera, P., Marsden, A. J., Laker, Z. P. L., Constantinescu, G. C., Kandyba, V., Barinov, A., Hine, N. D. M., Xu, X. D., Cobden, D. H., Determination of band offsets, hybridization, and exciton binding in 2D semiconductor heterostructures. *Sci. Adv.* **2017,** *3*, e1601832.

37. Chen, Z. H., Luo, J. W., Wang, L. W., Revealing angular momentum transfer channels and timescales in the ultrafast demagnetization process of ferromagnetic semiconductors. *Proc. Natl. Acad. Sci. U.S.A.* **2019,** *116*, 19258-19263.

38. He, J. J., Li, S., Bandyopadhyay, A., Frauenheim, T., Unravelling Photoinduced Interlayer Spin Transfer Dynamics in Two-Dimensional Nonmagnetic-Ferromagnetic van der Waals Heterostructures. *Nano Lett.* **2021,** *21*, 3237-3244.

39. Chen, J., Bovensiepen, U., Eschenlohr, A., Müller, T., Elliott, P., Gross, E. K. U., Dewhurst, J. K., Sharma, S., Competing Spin Transfer and Dissipation at Co/Cu(001) Interfaces on Femtosecond Timescales. *Phys. Rev. Lett.* **2019,** *122*, 067202.

40. Wang, G., Robert, C., Glazov, M. M., Cadiz, F., Courtade, E., Amand, T., Lagarde, D., Taniguchi, T., Watanabe, K., Urbaszek, B., Marie, X., In-Plane Propagation of Light in Transition Metal Dichalcogenide Monolayers: Optical Selection Rules. *Phys. Rev. Lett.* **2017,** *119*, 047401.

41. Sjöstedt, E., Nordström, L., Noncollinear full-potential studies of γ-Fe *Phys. Rev. B* **2002,** *66*, 014447.

42. Kresse, G., Furthmuller, J., Efficient Iterative Schemes for Ab Initio Total-Energy Calculations Using a Plane-Wave Basis Set. *Phys. Rev. B* **1996,** *54*, 11169-11186.

43. Blöchl, P. E., Projector Augmented-Wave Method. *Phys. Rev. B* **1994,** *50*, 17953-17979.

44. Perdew, J. P., Burke, K., Ernzerhof, M., Generalized Gradient Approximation Made Simple. *Phys. Rev. Lett.* **1996,** *77*, 3865.

45. Grimme, S., Antony, J., Ehrlich, S., Krieg, H., A Consistent and Accurate Ab Initio Parametrization of Density Functional Dispersion Correction (DFT-D) for the 94 Elements H-Pu. *J. Chem. Phys.* **2010,** *132*, 154104.

46. Huang, C. X., Feng, J. S., Wu, F., Ahmed, D., Huang, B., Xiang, H. J., Deng, K. M., Kan, E. J., Toward Intrinsic Room-Temperature Ferromagnetism in Two-Dimensional Semiconductors. *J. Am. Chem. Soc.* **2018,** *140*, 11519-11525.

47. Dewhurst, J. K., Sharma, S. et al. 2022, URL elk.sourceforge.net.